

Probing of noisy environments by dynamical decoupling

Dieter Suter

Fakultät Physik, Technische Universität Dortmund, D-44221 Dortmund, Germany

Filippo Caruso

*Department of Physics and Astronomy, University of Florence,
via G. Sansone 1, I-50019 Sesto Fiorentino, Italy*

Nir Bar-Gill

Departments of Applied Physics and Physics, Hebrew University of Jerusalem, Jerusalem, Israel

The technique of dynamical decoupling can generate filters for environmental noise that allow one to analyze its characteristic properties. Machine learning methods could enhance the extraction of information on the analysed noise spectra. Moreover, connections with optimal control theory can also be stated. In this regard, this report summarises the underlying physics, the formalism of spectral filtering, machine learning and control theory, the data analysis and some experimental considerations, namely advanced composite pulse techniques to enable control of noisy and inhomogeneously broadened systems.

I. MOTIVATION AND PRINCIPLES

The motivation for the PATHOS research project stems from the fact that no quantum system can be completely isolated from its environment. These environments are, in general, dynamical systems, i.e. they evolve in time, and they interact with the quantum system under study (to which, in the following, we will simply refer as “the system”) in different ways. The environment dynamics are typically characterized as random processes and their interaction with the system as noisy.

The main subject of this report is how the characteristics of the noise can be probed by suitable control operations applied to the system and what types of information about the environment can be obtained by such procedures.

The two main motivations for a detailed analysis of the noise properties are the following:

- To develop techniques that reduce the unwanted effect of the noise on the system of interest [1–3]
- To extract useful information about the environment that generates the noise [4–11].

In this report we focus on nuclear spin systems in different contexts: NMR, MRI or optically detected magnetic resonance of individual nuclear and electronic spins. In the context of MRI, the different relaxation times are determined by environmental noise and they offer the best option for contrast between different types of tissue as well as for assessing the health status and physiological properties of different tissues [12, 13]. In the quantum technologies framework, knowledge of the properties of the environmental noise can be helpful for assessing and mitigating its deleterious effect on the superposition

states that are the essential ingredients of most quantum technologies.

Modifying the spectral distribution can reduce the unwanted effects and extract useful information about the environment [1, 4]. Suitable modulation schemes can also generate back-action on the environment: The modulated interaction drives not only the system, but equally the environmental degrees of freedom. It can therefore be used, e.g., to control nuclear spins that are coupled to an electron spin via hyperfine interaction [14]. The modulated hyperfine coupling can then be used to drive the nuclear spins, with a much higher efficiency than what can be achieved by direct control via radio-frequency pulses [15–18]. Modulation can be pulsed such as dynamical decoupling (DD) [1, 19, 20] or continuous control fields [21, 22]. For some systems, at least partial information about the noise spectrum can be extracted from variations of the Hahn echo [23]. DD schemes will be specifically addressed in this report, including realizations based on advanced composite pulses (building upon rapid adiabatic passage techniques) to enable control and sensing in noisy environments and inhomogeneously broadened systems [24].

II. FILTER FUNCTION

The effect of the DD sequence on the environment can be described both in the time domain, where the pulses of the DD sequence are designed to invert the system-environment (SE) interaction, or in the frequency domain through the Fourier transform of the so-called time-domain modulation function, which is also known as *filter function*.

In the time domain, the modulation function can be writ-

ten as

$$f(t) \equiv \frac{\text{Tr} [S_z U(t) S_z U^\dagger(t)]}{\text{Tr} [S_z^2]}. \quad (1)$$

Here, S_z is the system operator that allows for the coupling with the environment, and

$$U(t) \equiv \mathcal{T} \exp \left[-i \int_0^t \mathcal{H}^c(t') dt' \right] \quad (2)$$

is the propagator generated by the control operations. For the generic case of a DD sequence with ideal δ -function inversion pulses, the modulation function alternates between ± 1 at the instances where the refocusing pulses are applied.

In the frequency domain, the Fourier transform $F(\omega) = \mathcal{F}\{f(t)\}$ of the modulation function $f(t)$ or its square modulus $|F(\omega)|^2$ are known as the Filter function, which describes how much of the noise is effectively transferred to the system - an approach borrowed from electronic filter theory [25].

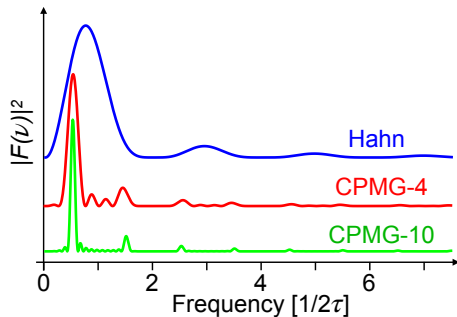


FIG. 1: Filter functions for different echo sequences.

For the Hahn-echo, the filter function can be written as

$$|F_{\text{Hahn}}(\omega, T)|^2 = \frac{4}{\pi\omega} \sin^2 \frac{\omega T}{2} (1 - \cos \omega T), \quad (3)$$

as shown by the top trace in figure 1. At low frequency, $\omega T \rightarrow 0$, the filter function approaches zero, $F_{\text{Hahn}}(\omega T) \rightarrow 0$, indicating that the Hahn-echo can refocus low frequency components completely.

III. THE CPMG SEQUENCE AS A FILTER

Using a larger number of control pulses allows one to fine-tune the spectral filter function. The simplest choice for this approach is to repeatedly apply inversion pulses, as first suggested by Carr and Purcell [19]. The resulting filter functions for 4 and 10 inversion pulses are shown in the lower traces of figure 1. They consist of a series of sinc functions at odd multiples of $1/2\tau$, with the amplitudes of the higher harmonics decreasing quadratically. The width of each peak is determined by $1/2N\tau$; it therefore gets progressively narrower with increasing total measurement time. In extreme cases, this measurement time

has been extended to hours, which allows frequency resolution in the μ Hz range [26]. When many DD cycles are applied to the system, the filter function becomes a sum of δ -functions and the decoherence rate is given by a discrete sum of spectral densities. A judicious choice of the DD sequence thus allows one to probe the environmental spectral density at well defined frequencies.

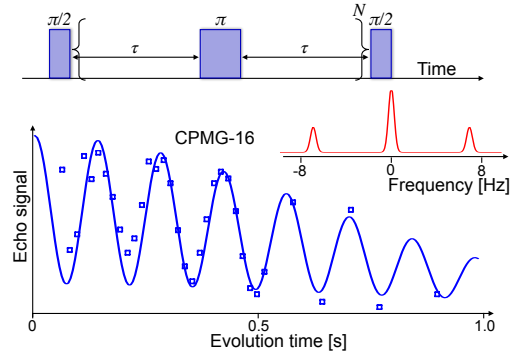


FIG. 2: Modulation of the spin echo in a CPMG sequence due to J -couplings. The top trace shows the corresponding pulse sequence and the inset the resulting spectrum, obtained as the Fourier transform of the fitted modulation function.

Figure 2 shows the pulse sequence, together with a specific application: Here, the system consists of a set of 3 identical spins, which are coupled to 2 other identical spins via a coupling

$$\mathcal{H}_J = J I_z^1 I_z^2 \quad (4)$$

with $J = 7$ Hz. Since the system is subject to inhomogeneous broadening with a linewidth of ≈ 35 Hz, this interaction could normally not be resolved. The refocusing pulses eliminate the inhomogeneous interaction while the J -coupling survives and gives rise to the oscillations visible in the blue data points and the fitted curve. Taking the Fourier transform of this curve yields the spectrum shown in red.

While the sequence of equidistant, identical π -pulses used in the CPMG sequence is often sufficient, it can be generalized, e.g., by using blocks of pulses whose phases may be varied or the delays between the pulses are adjusted. These additional degrees of freedom can be used, e.g., to make the sequences robust with respect to experimental imperfections [27–31].

IV. SPECTRUM EXTRACTION

The example discussed in section III shows how a CPMG sequence can be used to detect the spectral characteristics from a single static interaction with a group of two spins $1/2$, where the spectrum consists of only 3 lines. In a general case, the spectrum can be broad and may not easily be parametrised. It then becomes necessary to use a broader approach. This section discusses how CPMG

sequences can be used to specifically probe very narrow frequency components of the noise and reconstruct the full spectral distribution from a series of such measurements.

If the CPMG sequence is applied for a time $2N\tau$ that is long compared to the noise correlation time, the filter function $F(\omega)$ can be approximated by a series of δ functions centered at integral multiples of $\omega_0 = \pi/\tau$. The decay of the coherence becomes then effectively exponential, with the dephasing rate

$$\frac{1}{T_2} = \sum_{k=1,3,\dots}^{\infty} A_k^2 S(k\omega_0). \quad (5)$$

The amplitudes of the Fourier series decay with the inverse of the harmonic index, $A_k \propto 1/k$. Since the series is infinite, the measurement of a single relaxation time probes the spectral density function at many different points. Inverting equation 5 is therefore not trivial, but it can be well approximated by a 2-step procedure [4]: a first step measures a finite number of points and reconstructs a first approximation of the spectral distribution from those measurements. In a second step, the tail of the spectral distribution is expanded into a suitable functional form.

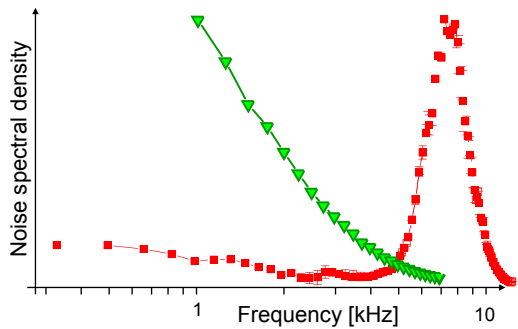


FIG. 3: Noise spectra of nuclear spin systems. The green data points were obtained from the stationary ensemble, while the red data points originate from a system that was driven at a rate of ≈ 7.7 kHz.

Figure 3 shows, as an example, the two noise spectra obtained from nuclear spin systems with the method described above. For the green data points, the spin system was evolving freely, driven by mutual spin flips under its internal spin-spin coupling. In this case, the maximum of the spectral density is at zero frequency. For the red data points, the spins were driven with an external control field that generated a rotation of ≈ 7.7 kHz, thus shifting the maximum to 7.7 kHz.

V. RECOUPLING

When an anisotropic solid is rotated, a spin with an anisotropic interaction, such as chemical shift, experiences a time-dependent Hamiltonian that can be written

as [32]

$$\mathcal{H}^r = S_z[(A + B(\cos \omega_r t - \varphi_1) + C(\cos 2\omega_r t - \varphi_2))] \quad (6)$$

where the parameters A , B , C , φ_1 , and φ_2 depend on system parameters like the orientation and anisotropy of the tensor as well as on experimental parameters like the orientation of the rotation axis. Figure 4 shows the

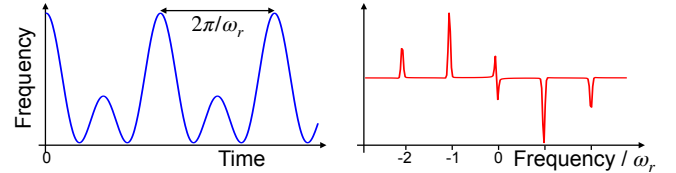


FIG. 4: Instantaneous frequency of the spin in a rotating anisotropic body (left) and the resulting spectrum (right) in units of ω_r .

evolution of the frequency defined by equation (6) during the rotation.

The goal of recoupling operations is to partly recover the time-dependent terms $\propto B, C$, which average to zero under fast rotation, $\omega_r \gg B, C$. This can be achieved by rotor-synchronized pulses, which invert the Hamiltonian at least twice per period. A $2\times$ per rotor period inversion means that the second term in Eq. (6) averages to

$$\begin{aligned} B_2 &= \frac{\omega_r B}{\pi} \int_{t_0}^{t_0 + \pi/\omega_r} \cos(\omega_r t - \varphi_1) dt \\ &= -\frac{B}{\pi} \sin(\omega_r t - \varphi_1) \Big|_{t_0}^{t_0 + \pi/\omega_r} \\ &= -\frac{B}{\pi} [\sin(\omega_r t_0 + \pi - \varphi_1) - \sin(\omega_r t_0 - \varphi_1)] \\ &= B \frac{2}{\pi} \sin(\omega_r t_0 - \varphi_1). \end{aligned} \quad (7)$$

Depending on the phase $\sin(\omega_r t_0 - \varphi_1)$, the recoupled value of the first harmonic term B can therefore assume values between $[-2/\pi \dots 2/\pi]$. The maximal value is obtained for $\omega_r t_0 = \varphi_1 + \pi/2$. To recover the second-harmonic term C , more pulses per period are required. A suitable sequence consists of four pulses at times $t_0 + \{0, 1, 2, 3\}\pi/(2\omega_r)$. The resulting average is

$$\begin{aligned} C_2 &= \frac{2\omega_r C}{\pi} \int_{t_0}^{t_0 + \pi/2\omega_r} \cos(2\omega_r t - \varphi_2) dt \\ &= -\frac{C}{\pi} \sin(2\omega_r t - \varphi_2) \Big|_{t_0}^{t_0 + \pi/2\omega_r} \\ &= -\frac{C}{\pi} [\sin(2\omega_r t_0 + \pi - \varphi_2) - \sin(2\omega_r t_0 - \varphi_2)] \\ &= C \frac{2}{\pi} \sin(2\omega_r t_0 - \varphi_2). \end{aligned} \quad (8)$$

The average covers the same range as B_2 and the maximum is attained for $2\omega_r t_0 = \varphi_2 + \pi/2$. Other options include the use of multiple pulses to recover the anisotropic information, but multiplied by a scaling factor [33].

This recoupling procedure can also be expressed in terms of a spectral filter: The rotation generates a noise spectrum that consists only of a δ -function at ω_r for the term proportional to B . The pulses modulate this time dependence with a filter function that alternates between ± 1 , with the same period as the rotation. In the frequency domain, this corresponds to a series of δ -functions at odd multiples of ω_r , with amplitudes that decrease with the harmonic order n as $1/n$.

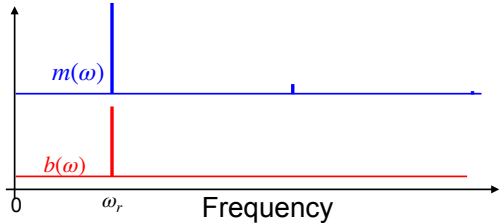


FIG. 5: Spectra of the rotation and the filter function from a pair of refocusing pulses.

Figure 5 compares the following two spectra

$$\begin{aligned} b(\omega) &= B_2 \mathcal{F}\{\cos(\omega_r t - \varphi_1)\} \\ m(\omega) &= |\mathcal{F}\{f(t)\}|^2. \end{aligned}$$

The convolution $b * m$ of these two functions has a component at $\omega = 0$, which corresponds to the integral (7):

$$B_2 = (b * m)(\omega = 0).$$

An important case is that of spins with dipolar couplings between them. The interaction is a second rank tensor in spin as well as in real space and therefore undergoes a modulation similar to (6). We consider a pair of dipolar-coupled spins that is rotated around an axis inclined by an angle θ from the direction of the static magnetic field. The internuclear vector is oriented at an angle α from the rotation axis. Neglecting an initial phase, the angle between the magnetic field and internuclear vector is then

$$\beta(t) = \theta + \alpha \cos(\omega_r t). \quad (9)$$

In a strong magnetic field, the effective coupling constant is thus modulated as

$$d(t) = d_0(3 \cos^2 \beta - 1) = d_0(3 \cos^2(\theta + \cos(\omega_r t)) - 1). \quad (10)$$

For the transverse component of the two spins, this creates a noise spectrum with components at multiple values of the rotation frequency ω_r , as shown in Fig. 6. For this figure, the rotation axis is chosen to be at the magic angle, which causes the mean interaction, i.e., the time-independent component at $\omega = 0$ to vanish, while the components at ω_r and $2\omega_r$ remain. The situation is qualitatively different if multiple spins are coupled to each other by dipole-dipole interactions, since the corresponding operators do not commute and accordingly, the time average becomes nonzero, unless the spinning speed is sufficiently high.

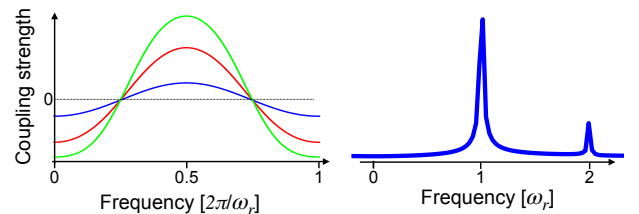


FIG. 6: Left: Time dependence of the effective coupling $d(t)$ during rotation around the magic angle for a pair of spins whose internuclear vector lies at an angle of $\alpha = 0.1$ (blue), 0.3 and 0.5 from the rotation axis. Right: The corresponding spectrum shows that at the magic angle, the average vanishes but the modulation generates a spectrum with frequency components at the rotation frequency and its second harmonic.

The frequency-domain picture bears an analogy to Floquet-theory and is sometimes helpful to analyze the cancellation of different modulation schemes, such as in the case of rotational resonance, where the sample rotation can cancel the modulation due to an energy difference between two non-equivalent spins [34]. While the rotation modulates the spatial coordinates of the Hamiltonian, it is also possible to modulate the spin coordinates by applying control pulses.

VI. EXPERIMENTAL CONSIDERATIONS

Since many of the experiments considered here use large numbers of RF pulses, it is important to take the effect of imperfections of these pulses into account [1]. As we have shown [27, 30], it is possible to design pulse sequences such that the flip angle errors due to inhomogeneous control fields or slowly-varying field amplitudes cancel over the sequence. Depending on the quantity to be measured, it is also possible to use adiabatic pulses, which are inherently robust against some perturbations [35]. Using these principles becomes increasingly important as the number of pulses (or, more generally) control operations increases.

Even if these mitigation measures are successful, and even more in cases where they are not, it is useful to assess the range of variations of the control field amplitude. We demonstrate this here for the case of an MRI system.

Figure 7 shows the measured distribution of the RF field strengths in the transverse plane of the 10 mm probe of the 14 T MRI system at TU Dortmund. Apparently the variation of the RF strength is of the order of $\pm 20\%$ for this probe. In the 25 mm probe, it is slightly larger and in clinical scanners, it can be at least twice this value.

We used these maps to estimate the effect of B_1 errors on the precision and accuracy of the measured T_1 , T_2 and T_2^* maps. We could identify different mechanisms that contribute to errors in the resulting maps and developed strategies for minimising them. One of the consequences of flip angle errors is that refocusing pulses generate co-

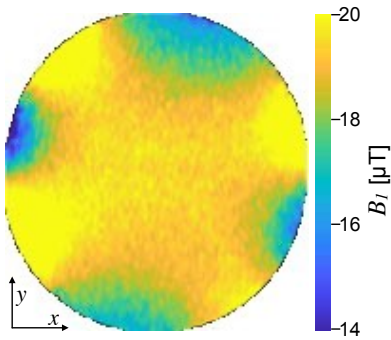


FIG. 7: Map of RF field strength in the xy -plane for a 10 mm sample tube in the 14 T MRI system.

herence which generates spurious signals. In many conventional MRI sequences, “crusher gradients” are placed around refocusing pulses to eliminate unwanted signal contributions. These have two disadvantages: they cause a loss of signal and they result in longer delays for the whole sequence. We have therefore reduced and partially eliminated these crusher gradients. For the reduction, we compared different parameters and searched for the “sweet point” where the artifacts were small and the unwanted effects were also acceptable. To eliminate them completely, we introduced phase cycling schemes that almost completely eliminated the artifacts.

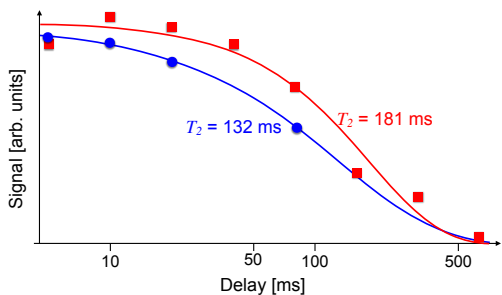


FIG. 8: Measured T_2 decay in a conventional experiment (red) and with phase cycling to eliminate spurious signal contributions. The experimental data are fitted to stretched exponentials.

Figure 8 shows the effect. The red data points were measured with a standard Hahn-echo experiment. Probably the most remarkable effect is that the first data point is not the largest value. These deviations could be eliminated by a phase cycle, which resulted in the blue data points. Both data sets were fitted with stretched exponentials. The resulting dephasing time for the corrected data was significantly shorter than for the original data.

VII. NOISE SPECTRA EXTRACTION VIA MACHINE LEARNING

Extracting information on quantum noise spectra can be very time consuming. In this paragraph, we propose the use of Machine Learning (ML) methods [36, 37] to speed up the sensing of noise features in quantum systems, as recently shown for example in Ref. [38].

ML is a cross-discipline field regarding the development of models from data. For example, in supervised learning [39, 40], a given data set of data is provided as input of the ML models that we aim to train, and to each input is associated a desired output. In this framework, the goal of the ML is to allow for the training of layered models such that the latter generalize to unseen input data, thus returning the correct output data. Instead, in Reinforcement Learning [41], the system consists in an agent that operates within an external environment; the agent improves his actions by learning from past experience.

Both supervised and reinforcement learning can be used for noise sensing purposes. The former can be used to leverage the information gained during the extraction of noise spectra to predict new spectra in similar contexts, but using less control pulses of the applied DD sequence. While very large sets of DD sequences are needed in current noise spectroscopy experiments, a ML model could be directly trained to predict an unknown noise spectrum by just resorting to a reduced set of DD sequences. In addition, reinforcement learning techniques can be adopted to choose better DD sequences, beyond to the inversion pulses that we have previously mentioned. In this context, the goal of the agent, acting in a simulated environment, would be to reconstruct the noise spectrum by means of the least possible DD sequences. This solution is expected to allow for new (and simpler) configurations of DD sequences.

A. Quantum noise classification

Here we provide more details on our recent application of deep learning techniques aimed to quantum noise classification [38]. In particular, we have exploited these tools to distinguish between Independent and Identically Distributed (i.i.d.) noise sequences and noise samples originated by a non-trivial memory kernel, characterized by specific time-correlation parameters.

To effectively present this novel approach and demonstrate its efficacy in discriminating Markovian and non-Markovian noise sources, we have focused on the single-particle case and specifically on the dynamics of a single quantum walker randomly moving on a graph \mathcal{G} [42–46], as generated by a stochastic Schrödinger equation. In this context, by training a properly-designed artificial neural network model via the probabilities that the quantum walker is in each node of the graph \mathcal{G} at discrete time instants, it has been possible to accurately discriminate between different noise sources and identify the possible

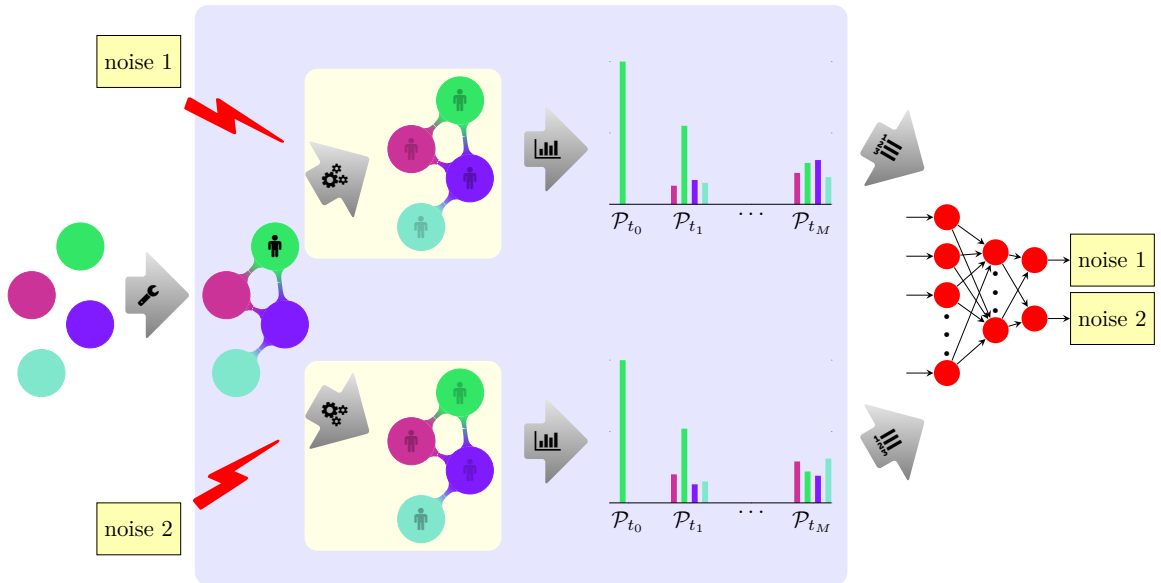


FIG. 9: Pictorial representation of the Machine Learning procedure for quantum noise classification as in Ref. [38]. Specifically, for a fixed set of nodes \mathcal{N} (coloured circles) and two types of noise sources, a random topology \mathcal{E} (edges linking the coloured circles) and a random initial distribution \mathcal{P}_{t_0} of the quantum system over the network (black pawn) determine the evolution of the analysed noisy dynamics for M consecutive steps (small yellow plate). After the quantum dynamics, all the distributions \mathcal{P}_{t_k} of the system, in correspondence of the $M + 1$ time instants t_k with $k = 0, \dots, M$, are collected and recorded with the noise type label. Then, a data set of N different realisations (big violet plate) is used to train a Machine Learning model (a neural network in the figure) that classifies the noise sources.

presence of noise time-correlation by only observing the single realisations of the stochastic quantum dynamics. Support Vector Machines (SVMs), Multi-Layer Perceptrons (MLPs) and Recurrent Neural Networks (RNNs) [47–50] were successfully trained on six data sets (each of them composed by 20 000 realisations) that have been properly generated to carry out binary classification of noisy quantum dynamics. Once trained, the proposed ML-models were able to reach a classification accuracy (defined by the number of correctly classified realisations over their total number) up to 97%. A pictorial representation of the proposed ML procedure is depicted in Fig. 9.

B. Machine learning for DD techniques

In the framework of DD-based noise spectroscopy, ML can allow for the reconstruction of the parameters of given noise spectral density functions $S(\omega)$, by possibly improving standard methods as the Álvarez-Suter protocol. Indeed, one may wonder if it is possible to reduce the computational burden of the noise inference process. Again, by making use of deep learning models with many intermediate layers, we could set as input to the ML model different time-dependent coherence-decay curves

$$C(t) \equiv \exp(-\chi(t)), \quad (11)$$

where $\chi(t)$ is the decoherence function, and as output the parameters of the noise spectral density. For instance, let

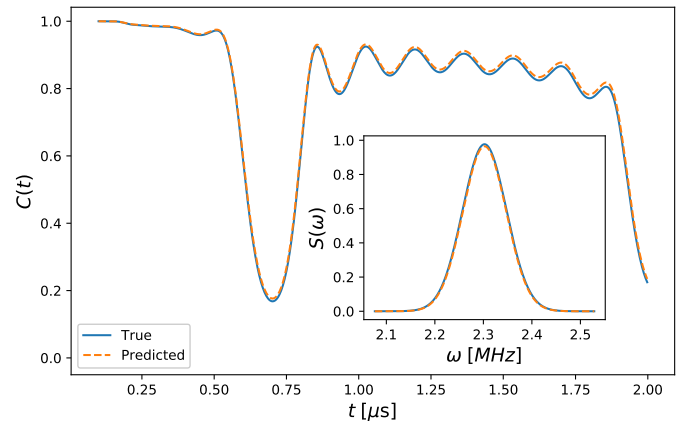


FIG. 10: Comparison between two coherence-decay curves $C(t)$, one (blue solid line) taken by the test set and given as input to the adopted ML model, and the other (orange dashed line) built from the predicted outputs (i.e., the noise parameters) of the ML model. Inset: Comparison between the test-set noise spectral density $S(\omega)$ and the predicted one, corresponding to the coherence-decay curves $C(t)$ above.

us consider that the noise spectral density is a Gaussian function. Then, $S(\omega)$ is defined by 4 parameters, i.e., the *offset* y_0 , the *amplitude* A , the *center* ω_c and the *standard deviation* σ such that

$$S(\omega) = y_0 + A \exp\left(-\frac{(\omega - \omega_c)^2}{2\sigma^2}\right). \quad (12)$$

We have thus generated a dataset of synthetic data containing a large number of coherence-decay curves obtained by varying the noise parameters in a suitable range, and using Carr-Purcell (CP) pulses as DD sequences. We recall that a CP sequence is composed by N equidistant π pulses (in our ML experiments $N = 8$), and enables the detection of monochromatic fields with periodicity commensurate with the interpulse delay time. In Fig. 10 we show a comparison between one sample of the synthetic dataset and the corresponding prediction provided by the ML model. Overall, a classification mean absolute error (MAE)

$$\eta = \frac{1}{4L} \sum_{i=0}^L |\hat{y}_0^{(i)} - y_0^{(i)}| + |\hat{A}^{(i)} - A^{(i)}| + |\hat{\sigma}^{(i)} - \sigma^{(i)}| + |\hat{\omega}_c^{(i)} - \omega_c^{(i)}| \quad (13)$$

of around 5% is achieved on the test set containing L elements, where $L \sim 5 \cdot 10^5$. In Eq. (13), all the values of the noise parameters (both generated and predicted ones) are normalized between 0 and 1. The MAE on $C(t)$ is 0.0064, while the one on $S(\omega)$ is 0.0074 – see the excellent agreement in Fig. 10.

During PATHOS we are planning to test our theoretical results on real sensing experiments.

VIII. ANALYTICAL ERROR SCALING IN CONTROLLING NOISY QUANTUM SYSTEMS

A quantum system is defined as open when it interacts with other systems or an environment with several degrees of freedom. Such an interaction radically changes the dynamics of the system, e.g., making the dynamics propagator as a non-unitary operator [51, 52].

In this context, quantum control theory investigates the possibility to steer a quantum system from an initial state to a desired one. For this reason, it has played and will play a key role in achieving breakthrough progress in quantum technologies. Outstanding results, as for example the generation of multi-component atomic Schrödinger cat states [53, 54], have been recently obtained thanks to the use of optimal control techniques.

To tackle efficiently the problem of steering a noisy quantum system in a desired way, a variety of solutions have been introduced. A widely used tool to mitigate the detrimental effect of the interaction of a system with its environment is provided by the dynamical decoupling of the system from the environment, as largely discussed in the previous sections of this report.

In a recently submitted paper [55], the error scaling of a quantum control problem has been studied as a function of both the noise level and control resources, from an information theoretical perspective.

To explain the novelties of Ref. [55] in connection with the topics addressed in this report, it is worth mentioning the Kofman-Kurizki universal formula [56]. The latter well describes the decay of unstable states into a continuum of

quantum levels, mimicking a macroscopic reservoir. The open dynamics originated by the interaction between a finite-dimensional quantum system and a reservoir leads to decoherence, which can be described by modeling the interaction with the reservoir as weak stochastic perturbations. Thus, the Kofman-Kurizki universal formula, under the hypothesis of weak coupling, predicts how a coherent manipulation of the quantum system modifies its decay rate into the reservoir [7].

In a similar context concerning open quantum systems, it has been proved (see Ref. [57]) that the minimal time needed to control a quantum system, bringing it to a given target state $\hat{\rho}$ with precision ε is equal to

$$T \geq -\frac{D_{\mathcal{W}}}{\mathcal{C}} \log_2(\varepsilon) \quad (14)$$

where \mathcal{C} denotes the channel capacity [52] of the control channel and \mathcal{W} is the set of reachable states with dimension $D_{\mathcal{W}}$. Eq. (14) has a clear interpretation: The amount of information necessary to solve a quantum optimal control problem with precision ε under finite channel capacity \mathcal{C} sets a time bound for the dynamics of the controlled system. In [55] it has been thus proved that the information-time bound of Eq. (14) for the error scaling and the Kofman-Kurizki universal formula for the quantum system decay rate are related.

Let us now sketch the arguments leading to this connection. In doing this, we can just consider a two-level system coupled to an arbitrary colored noise field, with Hamiltonian $H(t) = f(t)\sigma_x + \xi(t)\sigma_z$ where $f(t)$ denotes the control field and $\xi(t)$ is the colored noise field with spectral density $\varphi_\xi(\omega)$. Then, we denote the eigenstates of the Pauli operator σ_x by $|0\rangle$ and $|1\rangle$, and we suppose the system is initially prepared in the state $(|0\rangle + |1\rangle)/\sqrt{2}$. Under the influence of control and noise, the probability to keep the system in its initial state decays as

$$p(t) = \frac{1}{2}(1 + C(t)) \quad (15)$$

where $C(t) = e^{-\chi(t)}$ as in Eq. (11),

$$\chi(t) \equiv \int_0^\infty F(\omega)\varphi_\xi(\omega)d\omega \quad (16)$$

is the decoherence function, and $F(\omega)$ – as before – denotes the filter function that resembles the spectrum of the control pulse. According to DD methods, the control pulse is modulated to encode information on the noise field in the probability $p(t)$ or to minimize the decoherence function $\chi(t)$. For a continuous control field $f(t)$, one can introduce the accumulated phase $\theta(t) \equiv \int_0^t f(t')dt'$, and the pulse modulation functions $y(t) = \cos \theta(t)$ and $z(t) = \sin \theta(t)$, with the result that the filter function is given by

$$F(\omega) = \frac{4}{\pi} (|Y(\omega)|^2 + |Z(\omega)|^2)$$

with

$$Y(\omega) \equiv \int_0^t y(t') e^{i\omega t'} dt' \quad \text{and} \quad Z(\omega) \equiv \int_0^t z(t') e^{i\omega t'} dt'.$$

as in Ref. [8]. If the control pulse $f(t)$ is designed to protect the system in its initial state, the control error is provided by $\varepsilon = 1 - p$. Thus, after a fixed time T , it holds that

$$\varepsilon \approx \frac{1}{2} \chi(T) = \frac{1}{2} \int_0^\infty F(\omega) \varphi_\xi(\omega) d\omega \quad (17)$$

where $e^{-\chi(t)}$ has been approximated as $1 - \chi(t)$ for sufficiently small error values. To conclude, let us make also the following approximation: The filter function $F(\omega)$ is assumed to have support only around a central frequency ω_c and with a small bandwidth if compared to the power spectral density of the stochastic noise field. In this way,

$$\varepsilon \approx C_0 \varphi_\xi(\omega_c), \quad (18)$$

where C_0 is a constant term that depends on the specific choice of the filter function. We can now compare this result with the information theoretical limit

$$\varepsilon \geq 2^{-\frac{T}{D_{\mathcal{W}}} \int_{\omega_{\min}}^{\omega_{\max}} \log_2 \left(1 + \frac{\phi_f(\omega)}{\varphi_\xi(\omega)} \right) d\omega}, \quad (19)$$

generalizing the bound (14) in case of colored noise fields, where $\phi_f(\omega)$ denotes the power spectral density of the control pulse $f(t)$. In practical applications the control pulse is chosen such that the signal-to-noise ratio (evaluated in dB) exceeds a minimum threshold (at least 10-20 dB) that ensures a satisfactory value of the control fidelity \mathfrak{F} (more than 90%). This entails that

$$\log_2 \left(1 + \phi_f(\omega) / \varphi_\xi(\omega) \right) \approx \log_2 \left(\phi_f(\omega) / \varphi_\xi(\omega) \right)$$

such that

$$\varepsilon \gtrsim 2^{-\frac{T}{D_{\mathcal{W}}} \int_{\omega_{\min}}^{\omega_{\max}} \log_2 \left(\frac{\phi_f(\omega)}{\varphi_\xi(\omega)} \right) d\omega}. \quad (20)$$

Moreover, since the bandwidth of the control field is smaller than the frequency variation of the power spectral density $\varphi_\xi(\omega)$ associated to the noise field, the integral $\int_{\omega} \log_2 \left(\phi_f(\omega) / \varphi_\xi(\omega) \right) d\omega$ can be approximated by its integrand $\Delta\Omega \log_2 \left(C_1 / \varphi_\xi(\omega_c) \right)$, evaluated at the central frequency ω_c of the effective pulse modulation, together with the characteristic spectral width $\Delta\Omega$. Here, C_1 depends on the precise value and shape of $\phi_f(\omega)$. As a result,

$$\varepsilon \gtrsim \left(\frac{\varphi_\xi(\omega_c)}{C_1} \right)^{\frac{\Delta\Omega T}{D_{\mathcal{W}}}} \approx C_2 \varphi_\xi(\omega_c) \quad (21)$$

with $D = \Delta\Omega T$ chosen to be of the same order of magnitude than $D_{\mathcal{W}}$ and $C_2 = 1/C_1$ is a constant. This simply shows that the information-theoretical bound (19) leads to the same scaling of the error with the noise as the one obtained in Eq. (18) starting from the Kofman-Kurizki universal decoherence formula.

IX. USING ADIABATIC CHIRPED PULSES FOR ENHANCED SENSING

Magnetometry experiments require the measurement of a signal whose characteristics are related to a magnetic field to be sensed. Pulsed and continuous DD have already been applied for quantum memories and for sensing of oscillating (AC) fields in various systems, e.g., trapped ions, nitrogen-vacancy (NV) centers in diamond, rare-earth doped-solids [58–60]. However, the magnitude of the sensed signal is small in systems with large inhomogeneous broadening and field inhomogeneities also limit efficiency. Then, only a small fraction of the sensor atoms contribute to the signal due to the limited bandwidth of the control field.

Adiabatic chirped pulses perform robust population flips by rapid adiabatic passage (RAP) even in case of large inhomogeneous broadening, a weak driving field, and significant amplitude fluctuations [61, 62]. They have been applied for rephasing of atomic coherences [63] and combined with composite pulses [64] for high fidelity population transfer [65].

Here we propose sequences of phased RAP pulses for DD and sensing of an AC field [24]. The signal has a frequency of half the pulses' repetition rate and can be sensed in systems with large field inhomogeneity and varying transition frequencies, e.g., due to inhomogeneous broadening or different atom orientations with respect to the quantization axis as with NV containing nanodiamonds in cells. The RAP sequences act as a double filter for DD, where the population transfer dur-

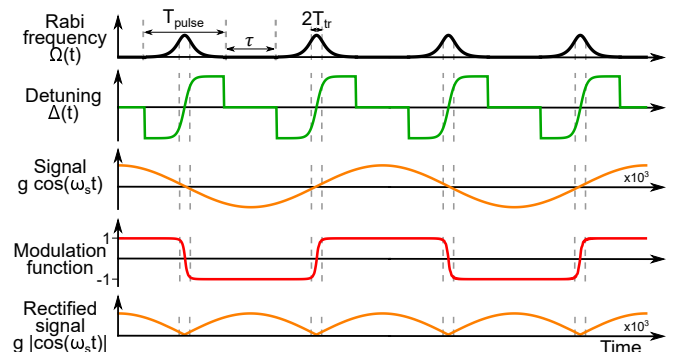


FIG. 11: (color online) Scheme for AC magnetometry with RAP pulses. The example follows the Allen-Eberly (AE) model [66] $\text{sech}[(t - t_{c,k})/T]$, where $t_{c,k}$ is the k -th pulse center, $\Delta(t) = (R/2) \tanh[(t - t_{c,k})/T]$, R is the chirp range, $T_{\text{pulse}} = 12T$. The pulses can be phase-shifted for improved performance. Our goal is to sense the amplitude g of an oscillating signal with $\omega_s = \pi/(T_{\text{pulse}} + \tau)$. The RAP pulses perform population transfer and modulate the signal. Usually, it is advantageous to take $\tau = 0$ and increase T_{pulse} to match ω_s , keeping T constant, as this improves adiabaticity without affecting the modulation function. The transition time $T_{\text{tr}} = 1/|\nu'(t_{c,k})| = 4T\Omega_0/R$ characterizes the time scale of population transfer. When $T_{\text{tr}} \ll T + \tau$, its effect can be neglected and the rectified signal takes the bottom shape.

ing a pulse rectifies the signal and partially removes frequency noise. The sudden changes in the mixing angle between the pulses act as fast π pulses in the adiabatic basis for additional noise compensation. Finally, we use the pulses' phases as control parameters to correct for other errors, e.g., due to non-adiabatic couplings. We demonstrate the superior performance of the RAP protocol with the XY8 sequence (RAP-XY8) in comparison to the widely used XY8 sequence [67] with rectangular pulses with the same peak Rabi frequency for realistic simulations.

Finally, we present convincing data from a demonstration experiment with relevance to applications in quantum sensing in an ensemble of NV centers in diamond. As the simulations and experimental data show, the RAP sensing protocol significantly outperforms the standard protocol with rectangular pulses.

A. Theory of RAP sensing

Our goal is to sense the amplitude of an AC field. We consider a two-state system, described by the Hamiltonian in the rotating-wave approximation

$$H_s(t) = -\frac{\tilde{\Delta}(t)}{2}\sigma_z + \frac{\tilde{\Omega}(t)}{2}\sigma_x + g\sigma_z \cos(\omega_s t + \xi), \quad (22)$$

where $\tilde{\Delta}(t) \equiv \Delta(t) - \Delta_\epsilon(t)$ is the detuning, which depends on the target detuning $\Delta(t)$ and an error $\Delta_\epsilon(t)$. The Rabi frequency is $\tilde{\Omega}(t) = \Omega(t)[1 + \epsilon_\Omega(t)] = \mu\tilde{B}(t)$, where $\epsilon_\Omega(t)$ is an error term. The amplitude, angular frequency, and initial phase of the sensed AC field are g , ω_s , and ξ . The Hamiltonian in the adiabatic basis is [61]

$$H_{\text{ad},s}(t) = -\frac{\tilde{\Omega}_{\text{eff}}(t)}{2}\sigma_z + g \cos(\omega_s t + \xi) \times [\cos(2\tilde{\nu}(t))\sigma_z + \sin(2\tilde{\nu}(t))\sigma_x], \quad (23)$$

where $\tilde{\nu}(t) = \arctan\left[-\frac{\tilde{\Delta}(t)}{\tilde{\Omega}(t)} + \sqrt{1 + \frac{\tilde{\Delta}(t)^2}{\tilde{\Omega}(t)^2}}\right]$ is the mixing angle (see [61]), $\tilde{\Omega}_{\text{eff}}(t) = \sqrt{\tilde{\Omega}(t)^2 + \tilde{\Delta}(t)^2}$, and we applied the adiabatic approximation ($|\tilde{\nu}'(t)| \ll \tilde{\Omega}_{\text{eff}}(t)$). One can obtain intuition about the effect of a RAP pulse by considering the evolution in the adiabatic and bare bases (see Fig. 12(a)).

Adiabatic evolution with population inversion is not necessarily optimal for DD due to noise in $\tilde{\Omega}_{\text{eff}}(t)$. Thus, we consider sequences of RAP pulses where the detuning shifts between the pulses, e.g., from large positive to large negative values, leading to sudden changes in the mixing angle by $\Delta\nu \approx \pi/2$. This is equivalent to applying instantaneous π pulses in the adiabatic basis, which compensate the noise in $\tilde{\Omega}_{\text{eff}}(t)$.

The time scale of detuning shifts is limited by the sampling rate of e.g., an arbitrary waveform generators, so sub-nanosecond shifts are readily achievable.

We incorporate such changes in the definition of our interaction basis, and obtain the Hamiltonian

$$H_{\text{int,tog},s}(t) = -\tilde{f}(t)g \cos(\omega_s t + \xi)\sigma_z, \quad (24)$$

where the modulation function $\tilde{f}(t) = f(t)\cos(2\tilde{\nu}(t))$ with $f(t) = -1$ ($f(t) = 1$) during the odd (even) pulses due to the sudden changes in the mixing angle between the pulses. We neglected fast oscillating terms, assuming $\omega_s \ll \tilde{\Omega}_{\text{eff}}(t)$ and $|\tilde{\nu}'(t)| \ll \tilde{\Omega}_{\text{eff}}(t)$. We note that $\tilde{f}(t)$ stays the same if $\Delta\nu = \pm\pi/2$ between two RAP pulses because $f(t)$ and $\cos(2\tilde{\nu}(t))$ change their signs simultaneously. Thus, the modulation function $\tilde{f}(t)$ is affected only by adiabatic changes in the mixing angle (see Fig. 11).

As the fast changes do not affect $\tilde{f}(t)$ (but only $f(t)$), the pulses can be truncated and separated by free evolution time τ (see Fig. 11), and we can sense the signal if $T_{\text{pulse}} + \tau = \pi/\omega_s$. However, it is usually preferable to use long pulses and $\tau = 0$ as this improves adiabaticity. If the RAP transition time is short, i.e., $T_{\text{tr}} \ll \pi/\omega_s$, where $T_{\text{tr}} = 2\tilde{\Omega}(t_c)/\tilde{\Delta}'(t_c)$ is defined in analogy to the transition time in stimulated Raman adiabatic passage [68], and t_c is the time of level crossing in the bare basis, the modulation function is approximately a step function (see Fig. 11).

Then, the Hamiltonian in Eq. (24) becomes $H_{\text{int,tog},s}(t) \approx -g|\cos(\omega_s t)|\sigma_z$ where we assumed $\xi = 0$ for maximum contrast and $\nu(t_0) = \pi/2$. Similarly to standard pulsed DD, the sensor qubit performs Ramsey oscillations where ($g \ll \omega_s$): $\eta(t) \equiv \int_0^t g|\cos(\omega_s t')|dt' \approx \frac{2}{\pi}gt$.

We can observe the signal stroboscopically in the bare basis after every second RAP pulse when the dynamic phase due to $\tilde{\Omega}_{\text{eff}}(t)$ (and its noise) is compensated by the instantaneous changes in the mixing angle, which act as π pulses in the adiabatic basis.

We note that these fast changes do not compensate non-adiabatic couplings, which usually commute with the Hamiltonian during the sudden change of the mixing angle. Additionally, $\Delta\nu$ might differ from $\pi/2$. We use the relative phases of the pulses to compensate for such and other errors, e.g., using the popular XY, KDD, or UR sequences [69]. These are based on composite pulses and improve population transfer and rephasing with imperfect RAP pulses [70].

We compare the performance of standard rectangular and RAP pulses by a numerical simulation for DD in a two-state system subject to magnetic noise and driving field fluctuations that follow an Ornstein-Uhlenbeck process [71] and are typical for experiments in NV centers [72]. We also assume an inhomogeneous broadening, leading to dephasing time of $T_2^* \approx 20$ ns and a Hahn echo $T_2 \approx 13$ μ s. We choose the Allen-Eberly model for RAP amplitude and detuning [66] due to its preferable adiabaticity.

Figure 12(b-e) shows the scheme and simulated evolution of the population in the $|1_y\rangle$ state in the bare basis for

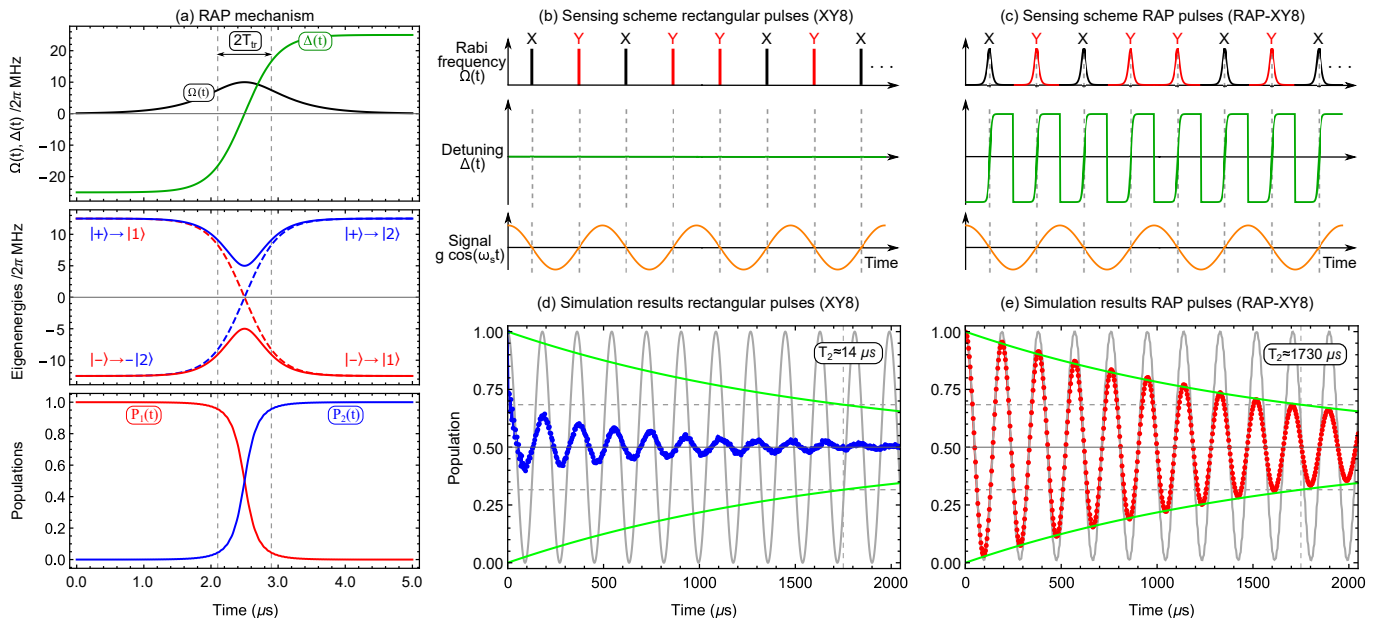


FIG. 12: (color online) (a) Mechanism of RAP: (*top*) Time dependence of the Rabi frequency and detuning for the AE model with $\Omega_0 = 2\pi \cdot 10$ MHz, chirp range $R = 2\pi \cdot 50$ MHz, and $T_{\text{pulse}} = 10T = 5 \mu\text{s}$. (*middle*) Time-dependence of the eigenenergies in the bare basis (dashed lines) and in the adiabatic (dressed) basis (solid lines). During the time evolution the composition of the adiabatic states changes due to a level crossing in the bare basis, which leads to population transfer. (*bottom*) Numerical simulation of population transfer between the bare states, which takes place on the time scale of the transition time $T_{\text{tr}} = 1/|\nu'(t_c)| = 4T\Omega_0/R = 0.4 \mu\text{s}$. Scheme for sensing with (b) the standard XY8 sequence of rectangular pulses and (c) with RAP-XY8. In both schemes the atoms are prepared initially in state $|1_y\rangle$, observed directly in the bare basis at time intervals of $8 \mu\text{s}$ with DD by (d) XY8 with rectangular pulses with $\Omega(t) = \Omega_0 = 2\pi \cdot 10$ MHz, duration $T_{\text{pulse}} = 50$ ns and pulse separation $\tau = 0.95 \mu\text{s}$, and (e) RAP-XY8 with chirped pulses that follow the Allen-Eberly model [66], with $\Omega_0 = 2\pi \cdot 10$ MHz, a target chirp range $R = 2\pi \cdot 95$ MHz, characteristic time $T = 0.2 \mu\text{s}$, pulse duration $T_{\text{pulse}} = 1 \mu\text{s}$, and pulse separation $\tau = 0$. The sensed field has an amplitude of $g = 2\pi \cdot 4.34$ kHz, initial phase $\xi = 0$ and angular frequency $\omega_s = 2\pi \cdot 0.5$ MHz. The peak Rabi frequency is the same in both protocols while the durations and pulse separation are chosen to match the $T_{\text{pulse}} + \tau = \pi/\omega_s$. The simulation assumes an inhomogeneous broadening with a Gaussian distribution with a full width at half-maximum of $2\pi \cdot 26.5$ MHz ($T_2^* = 20$ ns) and takes into account detuning and amplitude noise (see text). The light gray curve shows the theoretical evolution in an ideal system. The red curve shows the evolution with inhomogeneous broadening, frequency and amplitude noise. The coherence time is estimated $T_2 \approx 1.7$ ms and is more than two orders of magnitude higher with RAP pulses. The slight delay in the ideal, theoretical curve with RAP from $p = \cos(\eta(t))^2$ is mainly due to the non-instantaneous transition time, which is taken into account in the simulation.

sensing with rectangular and RAP pulses with identical peak Rabi frequency and the phases of the widely used XY8 sequence.

Due to the inhomogeneous broadening the contrast is lost quickly with the standard XY8, which has a $T_2 \approx 14 \mu\text{s}$ and is increased by more than two orders of magnitude to $T_2 \approx 1.7$ ms with RAP-XY8.

The remaining decay for RAP-XY8 is mainly due to high frequency components of the noise and imperfect adiabaticity. The coherence time with RAP-XY8 approaches the population lifetime of an NV center, which can reach up to 6 ms [73] and is not considered in the simulation.

B. Experimental demonstration

We experimentally demonstrate our scheme in an ensemble of NV centers in diamond. The measurements are performed in a home-built confocal fluorescence micro-

scope. The system and experimental setup are described in Fig. 13(a-b).

Modulated microwave control fields are created using an arbitrary waveform generator (AWG - Tektronix AWG70002A - 16 Gs). The measurements are performed on a standard-grade diamond sample (Element Six) with an NV density of ~ 10 ppb. The NV spin properties are measured to be $T_1 = 5.8 \pm 0.6$ ms, Hahn echo $T_2 = 390 \pm 301 \mu\text{s}$, and an inhomogeneous broadening of $2\pi \times (2.1 \pm 0.1)$ MHz.

First, we measured NV decoherence as a function of time by applying π pulses at a constant repetition rate, so the number of pulses increases with time. The NV is initially prepared in state $|0\rangle$ by optical pumping, then we apply a rectangular $\pi/2$ pulse for standard XY8 and half RAP for RAP-XY8. We carried out three sets of experiments: (i) at high Rabi frequency ($2\pi \times 5$ MHz); (ii) at high Rabi frequency with artificially added amplitude error for each sequence repetition, which follows a random

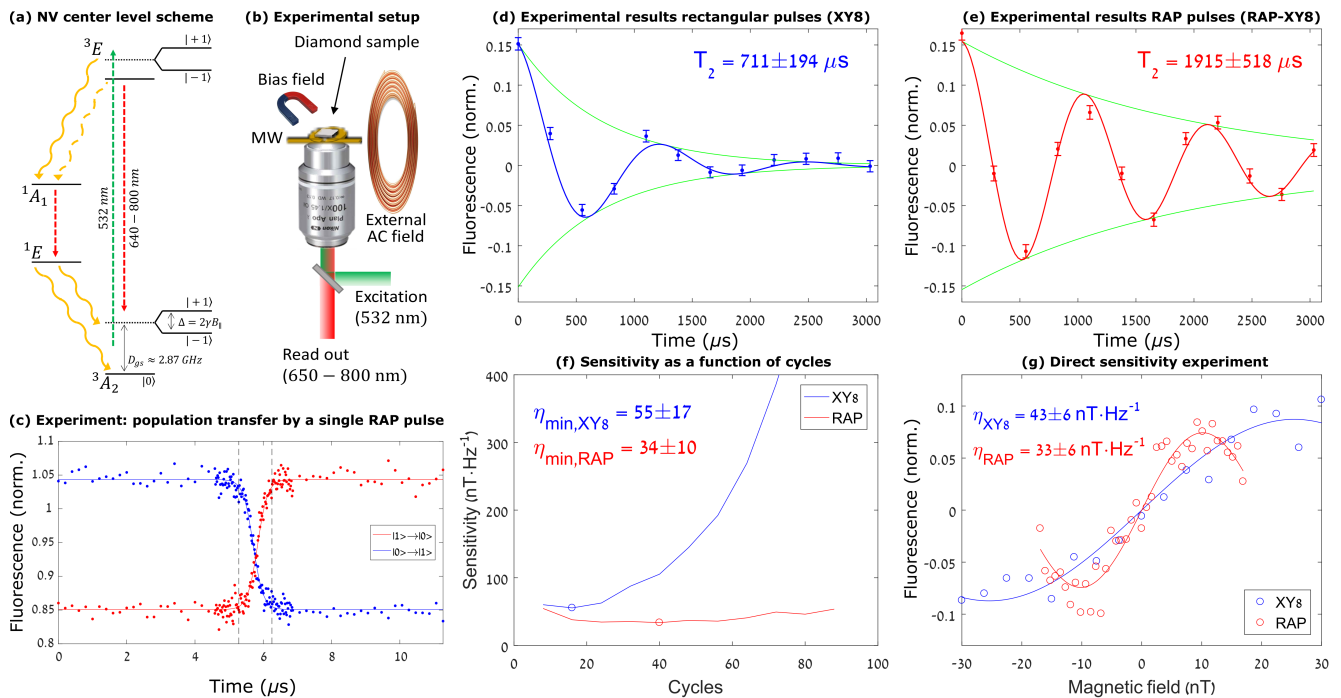


FIG. 13: (color online) (a) Energy level diagram of the NV center. The NV is excited with off-resonant green light (532 nm), coherently manipulated using microwave fields (resonant frequency of 2.87 GHz at zero magnetic field), and optically read-out through spin-dependent fluorescence between states $|0\rangle$ and $|\pm 1\rangle$. (b) Experimental setup scheme. (c) Measurement of population transition by a single RAP pulse. The actual transition time is short compared to the pulse duration (approx. 7%), as expected from theory. The dashed black line depicts the theoretical transition time $4\Omega_0 T/R$ around the pulse center. Coherence decay curves in presence of an artificial external magnetic field with amplitude of 25 nT and frequency of 14.5 kHz for the (d) XY8 sequence, which has a coherence time of $711 \pm 194\ \mu\text{s}$ and (e) for RAP-XY8 where the coherence time is extended to $1915 \pm 518\ \mu\text{s}$. (f) Sensitivity analysis as function of the number of free evolution-pulse-free evolution cycles, which shows the robust dependence for RAP and the high sensitivity for standard XY8. (g) Direct measurement of the sensitivity with optimized pulse parameters. A larger number of pulses in RAP cause lower contrast, but the important factor, the slope, is larger.

Gaussian distribution with a zero mean and a width of $0.2\Omega_0$; (iii) low Rabi frequency ($2\pi \times 1.7\text{ MHz}$). Each set included regular XY8 (“hard” pulses) and RAP XY8 sequences, and the measurement was performed twice for each: without an external field (a decoherence measurement) and with an AC magnetic field (acting as the signal to be sensed). The RAP pulse chirp range R and characteristic time T were optimized experimentally.

The AC magnetic signal field was generated using a home-built coil, driven by a function generator (Rigol 5252).

In the first series of experiments, we measured the coherence time (T_2) without an artificial AC field. The RAP XY8 sequence achieved $T_2 \simeq 1943\ \mu\text{s}$ for all experimental variants, i.e. it was robust to the added amplitude noise and when the Rabi frequency was lower than the bandwidth of the inhomogeneous broadening. Conversely, the coherence time for the regular XY8 was close to the one of RAP-XY8 only for the optimized high-Rabi experiment (without noise) at $T_2 \simeq 1811\ \mu\text{s}$. However, it degraded by about 40% with amplitude noise ($T_2 \simeq 1192\ \mu\text{s}$) and lower Rabi frequency ($T_2 \simeq 1057\ \mu\text{s}$). Thus, as expected

from theory, RAP-XY8 performed better for the non-ideal cases. We note that the coherence times of standard XY8 are expectedly longer in the particular sample in the experiment than in the simulation in Fig. 12 because the latter assumes much higher inhomogeneous broadening to highlight the broad applications of RAP-XY8.

Next, we performed quantum sensing experiments by adding an external magnetic field in order to characterize the magnetic sensitivity of our system under RAP and regular control pulses. The presence of the external field reduced the coherence time of the NV electron spin by $\sim 30\%$ using standard XY8 (see Fig. 13(d)). We attribute this effect to the rotation of the NV electron spin state in the XY plane of the Bloch sphere due to the field, so the system is more sensitive to pulse imperfections. While this effect should be negligible in the small-field limit, it does not adversely affect RAP sequences even for larger fields (Fig. 13(e)).

The sensitivity to an AC field is defined as $\eta = \frac{\sigma}{\partial S/\partial B} \sqrt{T}$, where σ is the standard deviation of the single point fluorescence data in the experiment, $\partial S/\partial B$ is the maximal slope in the curve of fluorescence signal vs. magnetic

field, and T is the time for a single measurement. Figure 13(f) shows the robust sensitivity, i.e., lower η , of the RAP-XY8 as a function of the number of pulses when extracted indirectly from the data. Direct measurements of the sensitivity in Fig. 13(g) under optimized conditions exhibit a $\sim 30\%$ improvement for RAP sequences over regular XY8. In the latter, we perform the comparison for the cases of minimum η in Fig. 13(f).

The standard XY8 is more sensitive to pulse errors and, thus, sensitivity is strongly suppressed for larger numbers of pulses. In contrast, RAP-XY8 is robust to pulse errors, leading to improved sensitivity, with a nearly constant value over a large range of applied pulses. This indicates that RAP sensing maintains an improved magnetic sensitivity over a broad frequency range of the sensed signal. We note that in our experiments the inhomogeneous broadening was relatively low (approx. $\simeq 2$ MHz), and thus we simulated a larger broadening by applying either weak driving (low Rabi frequency of $\simeq 1.7$ MHz) or added driving noise. The parameters chosen still correspond to limited broadening, yet clearly demonstrate a significant improvement (both in coherence time and magnetic sensitivity) of RAP compared to standard sensing.

C. Discussion

RAP sensing improves performance in comparison to standard pulsed sensing due to the greater bandwidth and robustness of RAP. The transition probability error for RAP depends on the pulse shape [74] and can be estimated $\epsilon_{\text{RAP}} \sim \epsilon_{\text{rect}} \frac{\omega_s^2}{\Omega_0^2}$ where $\epsilon_{\text{rect}} \sim \Delta_{\text{inh}}^2/\Omega_0^2$ is the rectangular pulse error.

Thus, RAP sensing improves performance when $\Omega_0 < \Delta_{\text{inh}}$ and $\omega_s \ll \Omega_0$. It is also less sensitive to amplitude variation. The frequency range of RAP sensing can be estimated as $\pi \left(\frac{b^2}{12\tilde{\tau}} \right)^{1/3} \ll \omega_s \ll \frac{\pi^2 \Omega_0^2}{4\Delta_{\text{inh}}}$, where the lower limit depends on the homogeneous broadening noise spectrum $S(\omega) = \frac{b^2}{\pi} \frac{1/\tilde{\tau}}{(1/\tilde{\tau})^2 + \omega^2}$, where $\tilde{\tau}$ is the correlation time of the environment and b is the bath coupling strength. The upper frequency limit can increase significantly by using appropriate pulse shapes or phased sequences that improve fidelity, e.g., the XY8 sequence.

When the the RAP transition time condition $T_{\text{tr}} \ll \omega_s/\pi$ is not fulfilled, there can be a slight shift in the amplitude

of the detected AC field in the noiseless case, which is straightforward to take into account (see Fig. 12).

Imperfect preparation and readout by standard $\pi/2$ pulses can be addressed by, e.g., using adiabatic half passage, robust composite $\pi/2$ pulses [64], adiabatic robust pulses [62], single-shot shaped pulses [75], pulses designed by optimal control [76].

Finally, we note that other methods [60] also allow for significant increase in the coherence times in NV centers in diamond, e.g., by applying strong driving fields or robust phased DD sequences. However, these typically require inhomogeneous broadening or amplitude errors to be smaller than the Rabi frequency, e.g., around ten percent. In contrast, RAP pulses are robust to a much broader range of errors.

X. CONCLUSIONS

Modifying the spectral composition of environmental noise has been developed over many decades in several related fields, such as magnetic resonance, optical spectroscopy and, most recently, quantum information. Two main driving forces behind these developments are the possibility

- to better characterize an environment that is itself not easily accessible to detailed investigations
- to allow for targeted and optimised reduction of unwanted effects of the noise on the system under study.

The latter may include the possibility to eliminate all but one components of the noise and thereby greatly increase the sensitivity for measuring this targeted component. This type of measurement is closely related to classical lock-in type measurements and can be optimised to virtually arbitrary frequency resolution [26].

In the present context, we are interested mostly in the information content that a noisy environment offers, e.g., for medical imaging. As a matter of fact, the techniques developed in quantum information to probe the noise spectral distribution offer a wide range of interesting options for improved medical diagnostics. Such topic will be addressed by us in our next future scientific investigations.

[1] D. Suter and G. A. Álvarez, *Rev. Mod. Phys.* **88**, 041001 (2016).
 [2] G. Kurizki, G. A. Alvarez, and A. Zwick, *Technologies* **5**, 1 (2017).
 [3] M. J. Biercuk, A. C. Doherty, and H. Uys, *Journal of Physics B: Atomic, Molecular and Optical Physics* **44**, 154002 (2011).
 [4] G. A. Álvarez and D. Suter, *Phys. Rev. Lett.* **107**, 230501

(2011).
 [5] T. Yuge, S. Sasaki, and Y. Hirayama, *Phys. Rev. Lett.* **107**, 170504 (2011), URL <http://link.aps.org/doi/10.1103/PhysRevLett.107.170504>.
 [6] M. M. Müller, S. Gherardini, and F. Caruso, *Sci. Rep.* **6**, 38650 (2016), URL <https://www.nature.com/articles/srep38650>.
 [7] A. Zwick, G. A. Álvarez, and G. Kurizki, *Phys. Rev.*

- Applied **5**, 014007 (2016), URL <https://link.aps.org/doi/10.1103/PhysRevApplied.5.014007>.
- [8] M. M. Müller, S. Gherardini, and F. Caruso, *Sci. Rep.* **8**, 14278 (2018), URL <https://www.nature.com/articles/s41598-018-32434-x>.
- [9] D. Goldwater, P. F. Barker, A. Bassi, and S. Donadi, *Phys. Rev. Lett.* **123**, 230801 (2019), URL <https://link.aps.org/doi/10.1103/PhysRevLett.123.230801>.
- [10] H.-V. Do, C. Lovecchio, I. Mastroserio, N. Fabbri, F. S. Cataliotti, S. Gherardini, M. M. Müller, N. Dalla Pozza, and F. Caruso, *New J. Phys.* **21**, 113056 (2019), URL <https://iopscience.iop.org/article/10.1088/1367-2630/ab5740>.
- [11] N. Dalla Pozza, S. Gherardini, M. M. Müller, and F. Caruso, *Int. J. Quantum Inf.* **17**, 1941008 (2020), URL <https://www.worldscientific.com/doi/abs/10.1142/S0219749919410089>.
- [12] P. A. Bottomley, T. H. Foster, R. E. Argersinger, and L. M. Pfeifer, *Med Phys* **11**, 425 (1984).
- [13] A. Zwick, D. Suter, G. Kurizki, and G. A. Álvarez, *Phys. Rev. Applied* **14**, 024088 (2020), URL <https://link.aps.org/doi/10.1103/PhysRevApplied.14.024088>.
- [14] J. E. Lang, D. A. Broadway, G. A. L. White, L. T. Hall, A. Stacey, L. C. L. Hollenberg, T. S. Monteiro, and J.-P. Tetienne, *Phys. Rev. Lett.* **123**, 210401 (2019), URL <https://link.aps.org/doi/10.1103/PhysRevLett.123.210401>.
- [15] J. Zhang, S. S. Hegde, and D. Suter, *Phys. Rev. A* **98**, 042302 (2018), URL <https://link.aps.org/doi/10.1103/PhysRevA.98.042302>.
- [16] J. Zhang, S. S. Hegde, and D. Suter, *Phys. Rev. Applied* **12**, 064047 (2019), URL <https://link.aps.org/doi/10.1103/PhysRevApplied.12.064047>.
- [17] J. Zhang, S. S. Hegde, and D. Suter, arXiv:1911.06371 [quant-ph] (2019).
- [18] S. S. Hegde, J. Zhang, and D. Suter, arXiv:1905.01649 [quant-ph] (2019).
- [19] H. Carr and E. Purcell, *Phys. Rev.* **94**, 630 (1954).
- [20] S. Meiboom and D. Gill, *Review of Scientific Instruments* **29**, 688 (1958).
- [21] J. Clausen, G. Bensky, and G. Kurizki, *Phys. Rev. Lett.* **104**, 040401 (2010), URL <https://link.aps.org/doi/10.1103/PhysRevLett.104.040401>.
- [22] J. Clausen, G. Bensky, and G. Kurizki, *Phys. Rev. A* **85**, 052105 (2012).
- [23] D. Farfurnik and N. Bar-Gill, *Phys. Rev. B* **101**, 104306 (2020), URL <https://link.aps.org/doi/10.1103/PhysRevB.101.104306>.
- [24] G. T. Genov, Y. Ben-Shalom, F. Jelezko, A. Retzker, and N. Bar-Gill, *Physical Review Research* **2**, 033216 (2020), ISSN 2643-1564, URL <https://link.aps.org/doi/10.1103/PhysRevResearch.2.033216>.
- [25] L. A. Zadeh, *Proceedings of the IRE* **50**, 856 (1962), ISSN 2162-6634.
- [26] J. M. Boss, K. S. Cujia, J. Zopes, and C. L. Degen, *Science* **356**, 837 (2017), ISSN 0036-8075, URL <http://science.sciencemag.org/content/356/6340/837>.
- [27] A. M. Souza, G. A. Álvarez, and D. Suter, *Phys. Rev. Lett.* **106**, 240501 (2011).
- [28] J. H. Shim, I. Niemeyer, J. Zhang, and D. Suter, *EPL (Europhysics Letters)* **99**, 40004 (2012), URL <http://stacks.iop.org/0295-5075/99/i=4/a=40004>.
- [29] G. A. Álvarez, A. M. Souza, and D. Suter, *Phys. Rev. A* **85**, 052324 (2012), URL <http://link.aps.org/doi/10.1103/PhysRevA.85.052324>.
- [30] A. M. Souza, G. A. Álvarez, and D. Suter, *Philosophical Transactions of the Royal Society A: Mathematical, Physical and Engineering Sciences* **370**, 4748 (2012), URL <http://rsta.royalsocietypublishing.org/content/370/1976/4748.abstract>.
- [31] M. A. Ali Ahmed, G. A. Álvarez, and D. Suter, *Phys. Rev. A* **87**, 042309 (2013), URL <http://link.aps.org/doi/10.1103/PhysRevA.87.042309>.
- [32] M. Maricq and J. S. Waugh, *J. Chem. Phys.* **70**, 3300 (1979).
- [33] Y. Yarim-Agaev, P. N. Tutunjian, and J. S. Waugh, *J. Magn. Reson.* **47**, 51 (1969).
- [34] M. H. Levitt, D. P. Raleigh, F. Creuzet, and R. G. Griffin, *J. Chem. Phys.* **92**, 6347 (1990).
- [35] G. T. Genov, Y. Ben-Shalom, F. Jelezko, A. Retzker, and N. Bar-Gill, *Phys. Rev. Research* **2**, 033216 (2020), URL <https://link.aps.org/doi/10.1103/PhysRevResearch.2.033216>.
- [36] S. Shalev-Shwartz and S. Ben-David, *Understanding machine learning: From theory to algorithms* (Cambridge university press, 2014).
- [37] T. Hastie, R. Tibshirani, and J. Friedman, *The elements of statistical learning: data mining, inference, and prediction* (Springer Science & Business Media, 2009).
- [38] S. Martina, S. Gherardini, and F. Caruso, Eprint arXiv:2101.03221 (2021).
- [39] I. Goodfellow, Y. Bengio, A. Courville, and Y. Bengio, *Deep learning*, vol. 1 (MIT Press Cambridge, 2016).
- [40] C. M. Bishop, *Pattern recognition and machine learning* (Springer, 2006).
- [41] R. S. Sutton and A. G. Barto, *Reinforcement learning: An introduction* (MIT Press, 2018).
- [42] Y. Aharonov, L. Davidovich, and N. Zagury, *Physical Review A* **48**, 1687 (1993).
- [43] J. Kempe, *Contemporary Physics* **44**, 307 (2003).
- [44] V. Kendon, *Mathematical structures in computer science* **17**, 1169 (2007).
- [45] S. E. Venegas-Andraca, *Quantum Information Processing* **11**, 1015 (2012).
- [46] N. Dalla Pozza and F. Caruso, *Physical Review Research* **2**, 043011 (2020).
- [47] C. M. Bishop, *Pattern recognition and machine learning* (springer, 2006).
- [48] I. Goodfellow, Y. Bengio, and A. Courville, *Deep learning* (MIT press Cambridge, 2016), <http://www.deeplearningbook.org>.
- [49] J. Schmidhuber, *Neural networks* **61**, 85 (2015).
- [50] Y. Goldberg, *Synthesis Lectures on Human Language Technologies* **10**, 1 (2017).
- [51] H. Breuer and F. Petruccione, *The Theory of Open Quantum Systems* (Oxford University Press, 2003).
- [52] F. Caruso, V. Giovannetti, C. Lupo, and S. Mancini, *Rev. Mod. Phys.* **86**, 1203 (2014), URL <https://journals.aps.org/rmp/abstract/10.1103/RevModPhys.86.1203>.
- [53] A. Omran and et al., *Science* **365**, 570 (2019).
- [54] C. Song and et al., *Science* **365**, 574 (2019).
- [55] M. M. Müller, S. Gherardini, T. Calarco, S. Montangero, and F. Caruso, Eprint arXiv:2006.16113 (2020).
- [56] A. Kofman and G. Kurizki, *Phys. Rev. Lett.* **87**, 270405 (2001), URL <https://journals.aps.org/prl/abstract/10.1103/PhysRevLett.87.270405>.

- [57] S. Lloyd and S. Montangero, *Phys. Rev. Lett.* **113**, 010502 (2014), URL <https://journals.aps.org/prl/abstract/10.1103/PhysRevLett.113.010502>.
- [58] L. Viola, E. Knill, and S. Lloyd, *Physical Review Letters* **82**, 2417 (1999), ISSN 0031-9007, URL <https://link.aps.org/doi/10.1103/PhysRevLett.82.2417>.
- [59] D. Suter and G. A. Álvarez, *Reviews of Modern Physics* **88**, 041001 (2016), ISSN 0034-6861, URL <https://link.aps.org/doi/10.1103/RevModPhys.88.041001>.
- [60] D. Farfurnik, A. Jarmola, L. M. Pham, Z. H. Wang, V. V. Dobrovitski, R. L. Walsworth, D. Budker, and N. Bar-Gill, *Physical Review B* **92**, 060301 (2015), ISSN 1098-0121, URL <https://link.aps.org/doi/10.1103/PhysRevB.92.060301>.
- [61] K. Rzazewski, *Science* **250**, 1603 (1990), URL <https://www.sciencemag.org/lookup/doi/10.1126/science.250.4987.1603>.
- [62] M. Garwood and Y. Ke, *Journal of Magnetic Resonance* (1969) **94**, 511 (1991), ISSN 00222364, URL <https://linkinghub.elsevier.com/retrieve/pii/S0022236491901371>.
- [63] S. Mieth, D. Schraft, T. Halfmann, and L. P. Yatsenko, *Physical Review A* **86**, 063404 (2012), ISSN 1050-2947, URL <https://link.aps.org/doi/10.1103/PhysRevA.86.063404>.
- [64] M. H. Levitt, in *Encyclopedia of Magnetic Resonance* (John Wiley & Sons, Ltd, Chichester, UK, 2007), URL <http://doi.wiley.com/10.1002/9780470034590.emrstm0086>.
- [65] G. T. Genov, D. Schraft, T. Halfmann, and N. V. Vitanov, *Physical Review Letters* **113**, 043001 (2014), ISSN 0031-9007, URL <https://link.aps.org/doi/10.1103/PhysRevLett.113.043001>.
- [66] L. Allen and J. H. Eberly (1975), URL <https://www.osti.gov/biblio/7365050>.
- [67] C. L. Degen, F. Reinhard, and P. Cappellaro, *Reviews of Modern Physics* **89**, 035002 (2017), ISSN 0034-6861, URL <http://link.aps.org/doi/10.1103/RevModPhys.89.035002>.
- [68] I. I. Boradjiev and N. V. Vitanov, *Physical Review A* **82**, 043407 (2010), ISSN 1050-2947, URL <https://link.aps.org/doi/10.1103/PhysRevA.82.043407>.
- [69] A. M. Souza, G. A. Álvarez, and D. Suter, *Philosophical Transactions of the Royal Society A: Mathematical, Physical and Engineering Sciences* **370**, 4748 (2012), ISSN 1364-503X, URL <https://royalsocietypublishing.org/doi/10.1098/rsta.2011.0355>.
- [70] G. T. Genov, D. Schraft, N. V. Vitanov, and T. Halfmann, *Physical Review Letters* **118**, 133202 (2017), ISSN 0031-9007, URL <http://link.aps.org/doi/10.1103/PhysRevLett.118.133202>.
- [71] M. C. Wang and G. E. Uhlenbeck, *Reviews of Modern Physics* **17**, 323 (1945), ISSN 0034-6861, URL <https://link.aps.org/doi/10.1103/RevModPhys.17.323>.
- [72] J.-M. Cai, B. Naydenov, R. Pfeiffer, L. P. McGuinness, K. D. Jahnke, F. Jelezko, M. B. Plenio, and A. Retzker, *New Journal of Physics* **14**, 113023 (2012), ISSN 1367-2630, URL <https://iopscience.iop.org/article/10.1088/1367-2630/14/11/113023>.
- [73] N. Bar-Gill, L. Pham, A. Jarmola, D. Budker, and R. Walsworth, *Nature Communications* **4**, 1743 (2013), ISSN 2041-1723, URL <http://www.nature.com/articles/ncomms2771>.
- [74] N. V. Vitanov, T. Halfmann, B. W. Shore, and K. Bergmann, *Annual Review of Physical Chemistry* **52**, 763 (2001), ISSN 0066-426X, URL <http://www.annualreviews.org/doi/10.1146/annurev.physchem.52.1.763>.
- [75] L. Van-Damme, D. Schraft, G. T. Genov, D. Sugny, T. Halfmann, and S. Guérin, *Physical Review A* **96**, 022309 (2017), ISSN 2469-9926, URL <http://link.aps.org/doi/10.1103/PhysRevA.96.022309>.
- [76] T. Nöbauer, A. Angerer, B. Bartels, M. Trupke, S. Rotter, J. Schmiedmayer, F. Mintert, and J. Majer, *Physical Review Letters* **115**, 190801 (2015), ISSN 0031-9007, URL <https://link.aps.org/doi/10.1103/PhysRevLett.115.190801>.